

Performance of Partially Deployed Spaceborne Ultra-Wideband Miura-Ori Apertures

MAXENCE CARVALHO¹ (Graduate Student Member, IEEE), AND JOHN L. VOLAKIS¹ (Fellow, IEEE)

Department of Electrical and Computer Engineering, Florida International University, Miami, FL 33174, USA

CORRESPONDING AUTHOR: M. CARVALHO (e-mail: mcarvalh@fiu.edu)

This work was supported by the Air Force Office of Scientific Research under Grant FA9550-19-1-0290.

ABSTRACT Reconfigurable and deployable antenna arrays are required communications and remote sensing onboard small satellites/CubeSats. There is also a need for packing before launch due to the limited payload space for exo-atmospheric deployments. In this context, origami-based aperture packing and unpacking is relevant and attractive for low-volume storage. However, after several physical morphing cycles, origami apertures may not maintain the performance exhibited by fixed apertures. That is, origami-based antenna arrays are likely to suffer from reduced gain and polarization purity. Therefore, physical effects caused by origami folding should be analytically incorporated into the design. This paper proposes a statistical analysis to study the gain performance of deployable ultra-wideband Miura-ori apertures by including geometrical errors inherent to a partially deployed state. A closed-form expression of the gain degradation is derived and verified using full-wave simulations.

INDEX TERMS Phased arrays, origami, TCDA, statistical analysis.

I. INTRODUCTION

THERE is a growing need for RF designs that are modular, deployable, and reconfigurable to accommodate smaller space platforms. Notably, nanosatellite launches have increased by 37 times since 2011 and will continue to grow over the next few years [1]–[2]. Also, 93% of nanosatellites downlink modules are spread across a nearly 27:1 frequency range, from 0.4 GHz to 10.5 GHz. UHF bands (400–402, 425 MHz, 435–438 MHz, 450–468 MHz, 900–915, 980 MHz) are typically used for downlink telemetry. Other bands, such as S-Band (2.2–2.5 GHz) and X-Band (8.2 GHz, 8.4 GHz, 10.5 GHz), are used for high-speed data transmission, remote sensing, radars, and satellite-to-satellite communications. Therefore, ultra-wideband arrays such as Tightly Coupled Dipole Arrays (TCDA) with > 20:1 contiguous bandwidth are attractive candidates for origami arrays [3]. Ultra-Wideband (UWB) apertures are also attractive due to their lightweight attributes. Furthermore, phased array antennas feature high gain, beam steering, and multi-beam capabilities, empowering miniature radars and remote sensing platforms with reduced payload costs [4]. In this context, origami-based antennas are attractive candidates to address the limited payload weight and space onboard

small satellites [5]–[6]. Specifically, deployable apertures, including the UWB aperture presented in Fig. 1, use origami-inspired deployment mechanisms [7]–[8]. However, such mechanisms suffer from mechanical errors due to manufacturing and tolerances that often lead to incomplete deployment and influence apertures performance.

To characterize apertures in such circumstances, a solution consists of considering randomly distributed errors in phases, amplitudes, and positions of the array elements to study their average contribution through statistical analyses. Typical statistical analyses are centered on element failure probabilities, phase and excitation errors caused by amplifiers, and phase shifters. The first such study was published in 1952. In [9], Ruze noted that random amplitude and phase errors add a constant power level that is proportional to the root mean square (RMS) of these errors. Concurrently, Bailin *et al.* proposed a characterization of the over-design necessary to minimize sidelobe levels (SLL) for linear array using a Dolph-Tchebychev distribution [10]. Elliott later completed this work for two-dimensional arrays subject to random mechanical and electrical excitation errors [11].

Furthermore, Rondinelli introduced a study on the beam pointing accuracy for the first time in [12]. Wang [13], [14]

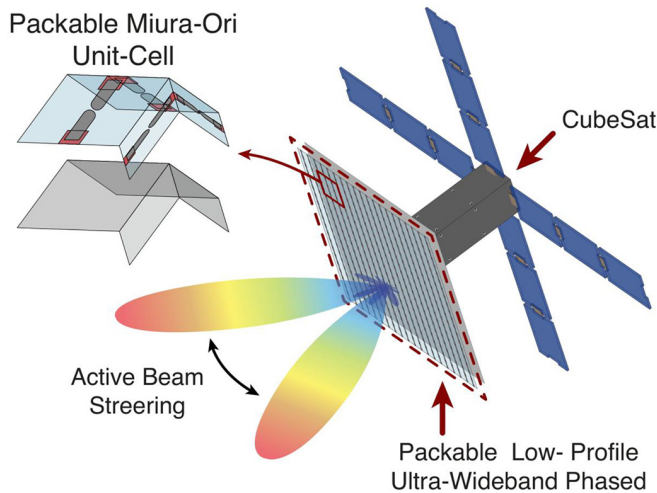


FIGURE 1. Illustration of a deployable ultra-wideband phased array onboard a CubeSat. The Miura-ori structure permits packing into a small volume. When deployed, these arrays enable beam steering.

concluded that for planar phased arrays with multiple sources of errors (amplitude, phase, element failure), the standard deviation of the element position errors must not exceed 1% of the operating wavelength to maintain < -10 dBi SLL. In recent years, more extensive studies on spaceborne mechanical array distortions were published [15]–[16]. Notably, the study by Ossowska *et al.* provided statistical simulations. In [16], both deterministic and random mechanical distortions were considered, and their impact was assessed for Synthetic Aperture Radar (SAR).

In the case of origami-based phased arrays, position errors are driven by the foldable structures. Rather than assuming position errors due to manufacturing and tolerances, it is more appropriate to consider random errors to be contained in substrates residual creases [17]–[19]. That is, position errors are typical to each origami structure [20]–[21].

This paper focuses on statistical analysis over elements positioning errors for Miura-fold TCDA. For this study, we propose a hinge-free unit cell, realizable with foldable materials like Kapton. The design demonstration operates from 0.35 GHz to 2.4 GHz and shows a 6.85:1 bandwidth with VSWR < 3 at broadside. The corresponding TCDA realized gain follows the theoretical $4\pi A/\lambda^2$ aperture gain (where A is the total aperture area) with a total efficiency of 87%, on average. Notably, we offer an analysis based on randomly distributed angular errors that are proper to our design (change in θ_m , shown in Fig. 2). It is observed that angular errors induce normally distributed phase errors. From our analysis, a closed-form expression of the gain degradation was derived as a function of the standard deviation of angular errors and the Miura-ori acute angle (see γ_m , shown in Fig. 2). This expression was verified with full-wave simulations for a 12×12 elements TCDA. To our knowledge, the proposed TCDA architecture is the first of its kind. Specifically, this is the first time that position

errors inherent to origami designs are considered for phased arrays. The derivation leading to the proposed expression is independent of frequency and can be used for any planar, low-profile, origami-based array such as slots or spirals. This communication is organized as follows. Section I introduces the design of the hinge-free Miura-fold unit cell and provides essential geometrical properties necessary to a good understanding of this work. Section II presents the derivation leading to expressions of the array elements phase errors. Section III gives a closed-form expression for the expected gain degradation caused by angular errors within the origami structure. Possible methods to compensate for such errors are also discussed.

II. TCDA ON MIURA-ORI LATTICE

A. PROPOSED MIURA-ORI UNIT CELL

The Miura-ori TCDA unit cell is comprised of four mirrored, anti-symmetric parallelogram surfaces (see left-most graphic in Fig. 2). While folding, each face motion is realized via two right-handed rotations in the global coordinate system (x, y, z) . Specifically, a rotation of $\pm\theta_m$ is done about the x -axis, followed by a rotation of $\pm(\frac{\pi}{2} - \xi_m)$ about the z -axis. As shown in Fig. 2, θ_m is the angle formed by the xy -plane and each face of the Miura-fold. In fact, the Miura-ori TCDA unit cell is a two-layered creased structure, comprising two mountain folds and two valley folds, such that

$$\tan \xi_m = \cos \theta_m \tan \theta_m \quad (1)$$

Another parameter of importance during the folding is γ_m , the parallelogram's acute angle. If $\gamma_m = 90^\circ$, the Miura-ori structure is an accordion-like structure folding only along the y -direction. For every other value of γ_m , the Miura-ori folds along both the x - and y -directions. Additional relations proposed by Schenk and Guest dictate the face centers positions [22]. Notably, the parameters H , S , L , and V define the Miura-ori unit cell's geometry as depicted in Fig. 2. Consequently, while folding, the Miura-ori TCDA unit cell fits in a cuboid of volume $2S \times (2L + V) \times (H + H_a)$, where

$$H(\theta_m, \gamma_m) = a \sin \theta_m \sin \gamma_m \quad (2)$$

$$S(\theta_m, \gamma_m) = b \frac{\cos \theta_m \tan \gamma_m}{\sqrt{1 + \cos^2 \theta_m \tan^2 \gamma_m}} \quad (3)$$

$$L(\theta_m, \gamma_m) = a \sqrt{1 - \sin^2 \theta_m \sin^2 \gamma_m} \quad (4)$$

$$V(\theta_m, \gamma_m) = \frac{b}{\sqrt{1 + \cos^2 \theta_m \tan^2 \gamma_m}} \quad (5)$$

Our proposed Miura-ori TCDA is composed of two layers: the ground plane layer and the dipole layer. Both layers fold simultaneously with the same Miura-ori parameters to avoid breaking. The dipoles (in grey, Fig. 2) and the overlapping pads (in red) are etched along the y -direction of the flat radiating sheet. When folding, radiation remains in the vertical polarization with minimal intended cross-polarization distortion. When flat, the distance between the ground

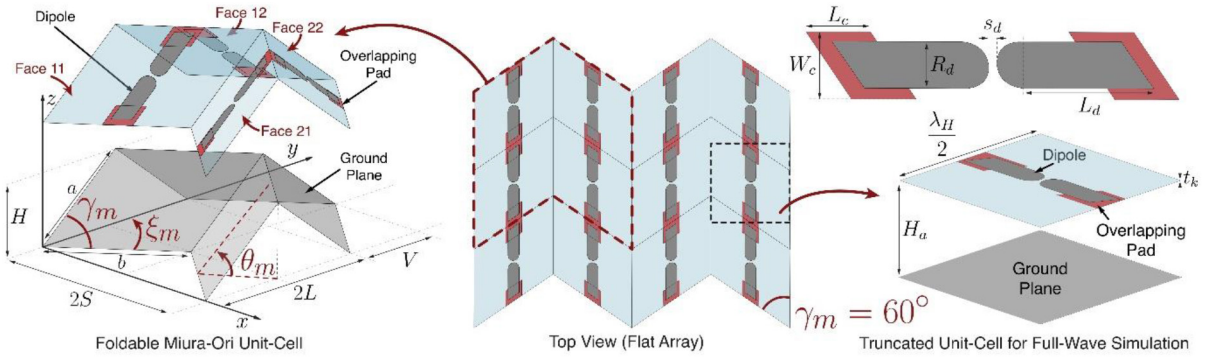


FIGURE 2. Proposed Miura-ori TCDA unit cell. The dipole elements and the overlapping pads are etched on the top layer. The ground plane constitutes the bottom layer. Both layers fold simultaneously while θ_m increases. In our case, $\gamma_m = 60^\circ$.

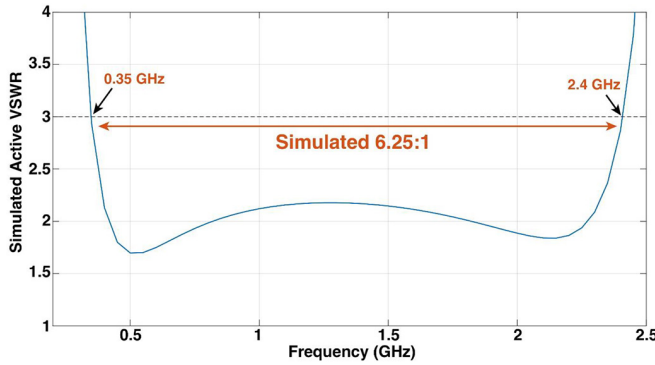


FIGURE 3. Simulated broadside VSWR of the proposed array unit cell showing 6.86:1 impedance bandwidth with VSWR < 3.

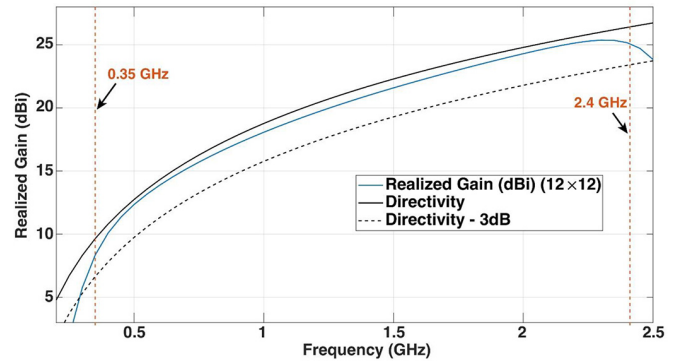


FIGURE 4. Simulated broadside realized gain of a 12×12 elements TCDA. The total efficiency is 87%, on average.

plane and the dipole sheet remains $H_a = \lambda_{high}/2.2$ where λ_{high} is the wavelength at the highest operating frequency. This spacing offers good low-frequency performance and excludes ground plane shorts for optimal bandwidth [23]. Furthermore, the inter-element spacing is based on the highest operating frequency. When the TCDA surface is flat, the element spacing along the x- and y-directions are equal, viz. $S(0, \gamma_m) = L(0, \gamma_m)$, and a square lattice is obtained with the following parallelogram side lengths

$$a = \frac{\lambda_{high}}{2}, \quad b = \frac{a\sqrt{1 + \tan^2 \gamma_m}}{\tan \gamma_m} \quad (6)$$

where the above parameters, a and b are depicted in Fig. 2. With the above geometrical description in mind, we proceed to simulate the Miura-ori TCDA performance.

B. INFINITE ARRAY SIMULATION OF MIURA-ORI TCDA

Infinite array simulations were carried out using the flat unit cell including Periodic Boundary Conditions (PBC) in Ansoft HFSS. In all simulations, the acute angle, θ_m , is set to $\theta_m = 60^\circ$. As seen in Fig. 3, the TCDA operates from 0.35 GHz to 2.4 GHz and shows a 6.85:1 bandwidth with VSWR < 3 at broadside. The corresponding realized gain of a 12×12 elements TCDA aperture is given in Fig. 4. The latter was obtained by combining the unit cell gain with the

array factor corresponding to a planar array of 144 elements. The final dimensions of the simulated TCDA are: $H_a = 5.4$ mm, $L_d = 29$ mm, $R_d = 14$ mm, $L_c = 12.5$ mm, $W_c = 16$ mm, $s_d = 1.3$ mm, and $t_k = 0.225$ mm. As seen, the co-polarization gain follows the theoretical $4\pi A/\lambda^2$ aperture gain (where A is the total aperture area). Notably, the total efficiency is 87%, on average.

III. POSITION ERROR ESTIMATES

A. RADIATING ELEMENT GEOMETRY VARIATION

For brevity, above and herewith, for any angle $\alpha \in [0, 2\pi]$, we set $C_\alpha = \cos \alpha$, $S_\alpha = \sin \alpha$, and $T_\alpha = \tan \alpha$. As depicted in Fig. 2 (left-most graphic), each dipole has its phase center located at the center of each parallelogram. While folding, the coordinates of the first element can be obtained using (2)-(5).

In the global coordinate system (x, y, z) , the position vector of the first radiating element is given by

$$\mathbf{p}_{11} = \left[\frac{S}{2}, \quad \frac{V+L}{2}, \quad H_a + \frac{H}{2} \right] \quad (7)$$

where H , S , L , and V are the Miura-ori parameters defined in (2)-(5). Also, $H_a = \lambda_{high}/2.2$ is the distance of the aperture from the ground plane. Fig. 5 depicts some of the arrays elements in the flat configuration. Using (2)-(7), the position

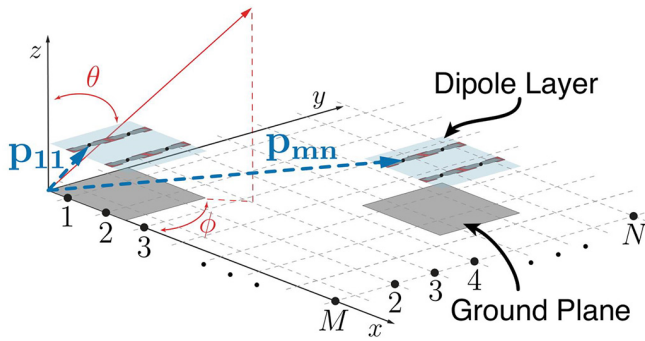


FIGURE 5. Deployed Miura-ori TCDA. The position vector of the mn^{th} element is p_{mn} . As seen, p_{mn} can be obtained using the array elements spatial periodicity mentioned in (2)-(7).

vector of the mn^{th} element center is given by

$$p_{mn} = p_{11} + [(m-1)S, (n-1)L, 0] \quad (8)$$

In this, $(m, n) \in [[1, N]] \times [[1, M]]$, and $(M, N) \in \mathbb{N}^2$ are the numbers of elements along the x- and y-directions, respectively.

When the array is perfectly flat (viz. error-free), the realized gain follows the curve presented in Fig. 4. However, in partial deployments, as in Fig. 6, the gain is reduced. Fig. 6b shows a typical Miura-ori TCDA structure fabricated using Kapton and FR4 substrates. Nylons screws are used to constrain the displacement of both layers when the array folds. Each layer (dipole layer and ground layer) was adjusted using the nylon screws. The aperture height was first measured using a caliper and fixed using a pair of nylon bolts screwed in opposite directions. The structure was fabricated as a prototype to assess its mechanical aspect. As expected, after multiple folding and unfolding cycles, the prototype's surface is permanently affected due to elastic hysteresis. This prototype is a particular case of the Miura-fold where $\gamma_m = 90^\circ$, folding only along the y-direction. Despite being a specific case, this accordion-like structure perfectly illustrates aperture errors and the following derivation remains valid for any γ_m value. Below, we proceed to quantify the gain errors due to element position errors. Because of the unit cell dimensions given in (6), minor angular errors will engender gain errors [14]. Based on previous studies and experience, it is fair to assume that most of the performance errors will be due to phase variations. Specifically, the non-flatness of the array surface would result in slight variations of the phase centers p_{mn} . Therefore, even if we assume the pattern (field-amplitude) to remain fairly constant, phase variation will have a more significant impact.

To obtain the engendered phase variations, we begin by considering the variation of the geometrical parameters given in (2)-(5). This is done by setting $\theta_m = \theta_{m0} + \delta\theta_m$ with $\theta_{m0} = 0$ (referring to a flat surface). We assume that $\delta\theta_m$ varies within $\pm 10^\circ (\pm \frac{\pi}{18})$. Such value is arbitrarily chosen after observation of the fabricated test piece. Specifically, for this specific prototype, the folding error was not exceeding $\pm 10^\circ$. However, for the following first-order

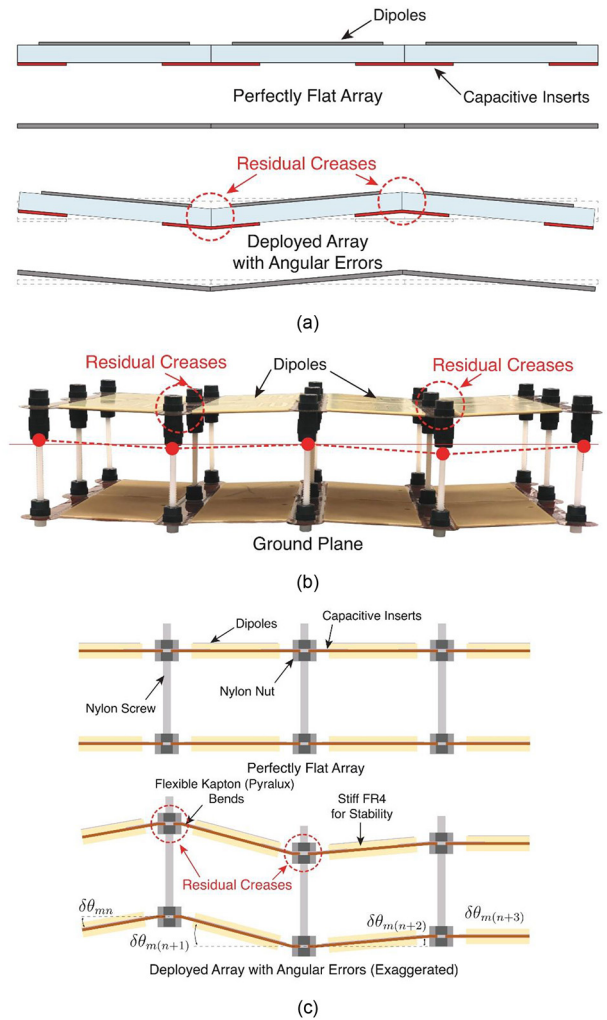


FIGURE 6. (a) Profile of a typical partially deployed spaceborne phased array. (b) Partially deployed proposed two-layered UWB array structure. This structure was fabricated to assess the elastic hysteresis of such array class and was not characterized from an RF point of view. (c) Graphical representation of the structure prototype showing different angular error for each element.

and second-order approximations, the relative error does not exceed 1% for angles up to $\pm 14^\circ$, and $\pm 37^\circ$, respectively. Replacing $\sin\delta\theta_m$ and $\cos\delta\theta_m$ in (2)-(5) with their Taylor series expansion, we have

$$S_x = x + \mathcal{O}(x^3) \text{ and } C_x = 1 - \frac{x^2}{2} + \mathcal{O}(x^4) \quad (9)$$

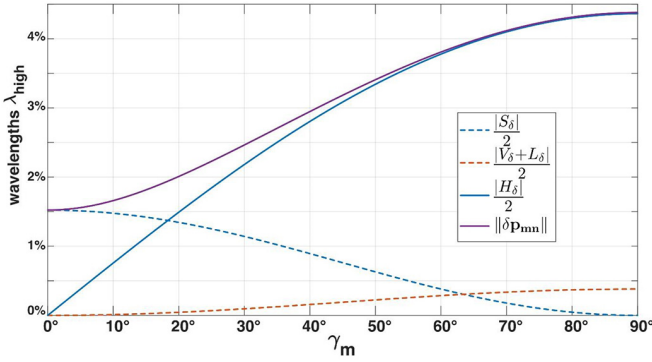
where $S_x = \sin x$ and $C_x = \cos x$. This leads to the following approximations

$$H(\delta\theta_m, \gamma_m) = \underbrace{0}_{H(0, \gamma_m)} + \underbrace{\frac{\lambda_{high}}{2} S_{\gamma_m} \delta\theta_m}_{t_H} + \mathcal{O}(\delta\theta_m) \quad (10)$$

H_δ

$$S(\delta\theta_m, \gamma_m) = \underbrace{\frac{\lambda_{high}}{2}}_{S(0, \gamma_m)} - \underbrace{\frac{\lambda_{high}}{4} \frac{1}{1 + T_{\gamma_m}^2} \delta\theta_m^2}_{t_S} + \mathcal{O}(\delta\theta_m^3) \quad (11)$$

S_δ


FIGURE 7. Comparison of δp_{mn} vs γ_m for the maximum angular error of $\delta\theta_m = 10^\circ$.

$$L(\delta\theta_m, \gamma_m) = \underbrace{\frac{\lambda_{high}}{2}}_{L(0, \gamma_m)} - \underbrace{\frac{\lambda_{high}}{4} S_{\gamma_m}^2 \delta\theta_m^2}_{t_L} + \mathcal{O}(\delta\theta_m^2) \quad (12)$$

L_δ

$$V(\delta\theta_m, \gamma_m) = \underbrace{\frac{\lambda_{high}}{2}}_{V(0, \gamma_m)} - \underbrace{\frac{\lambda_{high}}{4} \frac{T_{\gamma_m}^2}{1 + T_{\gamma_m}^2} \delta\theta_m^2}_{t_V} + \mathcal{O}(\delta\theta_m^2) \quad (13)$$

V_δ

From the above, the new position \mathbf{p}'_{mn} is of the form

$$\mathbf{p}'_{mn} = \mathbf{p}_{mn} + \underbrace{\left[\frac{S_\delta}{2}, \frac{V_\delta + L_\delta}{2}, \frac{H_\delta}{2} \right]}_{\delta \mathbf{p}_{mn}} = \mathbf{p}_{mn} + \delta \mathbf{p}_{mn} \quad (14)$$

where, $\delta \mathbf{p}_{mn}$ refers to the position error. From (14), we also note that S_δ contributes to the errors in the x-direction whereas L_δ and V_δ contribute to position errors in the y-direction. The vertical position errors are associated with H_δ . Fig. 7 compares the position errors for different acute angles γ_m for $\delta\theta_m = 10^\circ$.

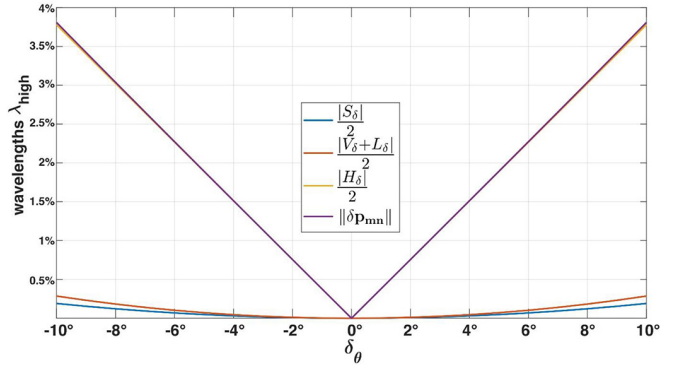
From Fig. 7, it is clear that for $\delta\theta_m = 10^\circ$, the contribution of H_δ is dominant, except for small γ_m values ($\gamma_m \leq 40^\circ$). However, to keep minimal array deformations, it is necessary to chose $\gamma_m \geq 40^\circ$. Therefore, the cases with smaller values of γ_m are not as relevant.

The importance of H_δ is also seen in Fig. 8 when $\gamma_m = 60^\circ$. For instance, when $\delta\theta_m = 10^\circ$, the contributions of the horizontal components (viz. proportional to S_δ , L_δ , and V_δ) correspond to only 0.5% of the wavelength at the highest operating frequency. However, the corresponding contribution due to H_δ is almost 4% of the wavelength at the highest operating frequency.

B. PHASE ERROR EXPRESSION

Denoting the array elements as $(m, n) \in [[1, N]] \times [[1, M]]$ and assuming that all the element patterns are identical, the far-field radiation pattern can be expressed as

$$f(\theta, \phi) = \sum_{m=1}^M \sum_{n=1}^N I_{mn} e^{jk \cdot (\mathbf{p}_{mn} + \delta \mathbf{p}_{mn})} \quad (15)$$


FIGURE 8. Comparison of δp_{mn} components as a function of the angular error $\delta\theta_m$ for $\gamma_m = 60^\circ$.

In the above, M and N denote the numbers of elements in the x- and y-directions, respectively, I_{mn} is the complex excitation of the mn^{th} element, \mathbf{p}_{mn} is the position vector of the mn^{th} element, and \mathbf{k} refers to the propagation vector expressed in the global coordinate system (x, y, z) . For a fixed direction (θ, ϕ) , \mathbf{k} is given by

$$\mathbf{k} = k[u, v, w] = \frac{2\pi}{\lambda}[u, v, w] \quad (16)$$

where, as usual, $u = S_\theta C_\phi$, $v = S_\theta S_\phi$, and $w = C_\theta$, and λ is the operational wavelength. Using (14)-(16), we can rewrite $f(\theta, \phi)$ as

$$f(\theta, \phi) = \sum_{m=1}^M \sum_{n=1}^N I_{mn} e^{jk(S(m-1)u + L(n-1)v)} \underbrace{e^{jk \cdot \delta \mathbf{p}_{mn}}}_{\text{Phase Error}} \quad (17)$$

In this, the phase error deviation is given by

$$k \cdot \delta \mathbf{p}_{mn} = k \underbrace{\left(-\frac{t_S}{2} u + \frac{t_V - t_L}{2} v \right)}_{\alpha(\theta, \phi)} \delta\theta_{mn}^2 + k \underbrace{\left(\frac{t_H}{2} w \right)}_{\beta(\theta, \phi)} \delta\theta_{mn} \quad (18)$$

In the above, the second-order contribution is referred as $\alpha(\theta, \phi)$, the first-order contribution as $\beta(\theta, \phi)$, and $\delta\theta_{mn}$ is now the small angle variation of the mn^{th} element. It is clear from (18) that the overall phase error depends on the variables u , v , and w . This means that both the first and the second-order components vary throughout the scanning region of the array. For instance, if $\theta \sim 90^\circ$, then $\beta(\theta, \phi) \sim 0$ and the second-order phase error is predominant.

Fig. 9 Shows the variation of $\alpha(\theta, \phi)/\beta(\theta, \phi)$ for a maximum angular deviation $\delta\theta_m = 10^\circ = 0.1745$ rad. It is noted that, if $\theta \in [0^\circ, 60^\circ]$ and $\phi \in [-180^\circ, 180^\circ]$, the second-order phase error is 20 to 200 times less important than the first-order error. As a consequence, we will assume that the phase error is due to $\beta(\theta, \phi)$ only. That is,

$$k \cdot \delta \mathbf{p}_{mn} \cong \left(\frac{t_H}{2} w \right) \delta\theta_{mn} \quad (19)$$

It is important to mention that the ratio $\alpha(\theta, \phi)/\beta(\theta, \phi)$ does not depend on the operating frequency. Consequently, the previous simplification remains valid for the ultra-wideband aperture presented in Section I.

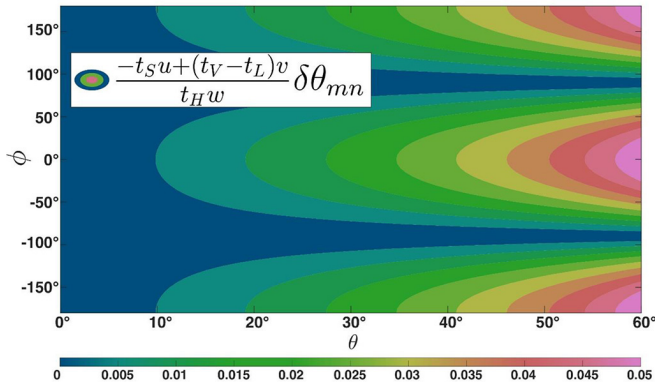


FIGURE 9. Variation of $\alpha(\theta, \phi)/\beta(\theta, \phi)$ for the maximum angular deviation of $\delta\theta_{mn} = 10^\circ = 0.1745$. Second-order components can be neglected throughout the scanning region where $(\theta, \phi) \in [0^\circ, 60^\circ] \times [-180^\circ, 180^\circ]$.

IV. GAIN OF PARTIALLY DEPLOYED MIURA-ORI TCDA

A. HYPOTHESES ON PHASE ERROR

In the following derivation, the angular error, $\delta\theta_{mn}$ is considered to be a random variable with a normal distribution around 0° , and a standard deviation σ_θ . We can support this choice by noting that the angular error is a sum of independent random contributions (e.g., fabrication errors, residual creases, inclination, deformation, weight distribution, mechanical constraints). As such, $\delta\theta_{mn}$ will have a Gaussian distribution. Furthermore, angular errors are assumed to be mutually independent. That is, the angular error of one element face does not influence the other array elements. In practice, this statement is more valid as the number of elements in the array increases.

B. AVERAGE GAIN DEGRADATION

Based on previous hypotheses, the radiated field pattern can be expressed by inserting (19) into (17). Next, by multiplying (17) with its complex conjugate and taking the statistical average, we have:

$$\overline{|f(\theta, \phi)|^2} = \sum_{m=1}^M \sum_{n=1}^N \sum_{p=1}^M \sum_{q=1}^N I_{mn} I_{pq}^* e^{jk(S(m-p)u + L(n-q)v)} \times e^{j(\psi_{mn} - \psi_{pq})} \quad (20)$$

In the above, $\phi_{mnpq}(u, v) = jk(S(m - p)u + L(n - q)v)$ is a deterministic quantity that represents the phase components of the error-free power pattern. On the other hand, ψ_{mn} is the random phase error engendered by the random folding error $\delta\theta_{mn}$. Specifically, from (20) we have:

$$\psi_{mn} = \underbrace{\left(\frac{2\pi}{\lambda} \frac{\lambda_{high}}{4} S_{\gamma_m} \right)}_{A_0} \delta\theta_{mn} \quad (21)$$

As $\delta\theta_{mn}$ is a normally distributed random variable with a standard deviation, σ_θ , the random variable ψ_{mn} also has a normal distribution with a standard deviation $\sigma_\psi = A_0\sigma_\theta$ for $A_0 > 0$. From (20), and a similar derivation as the one

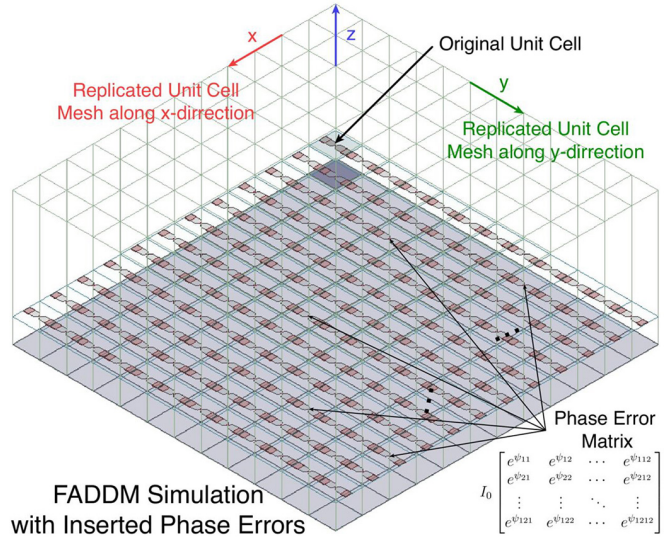


FIGURE 10. Simulation set-up of the Finite Array Domain Decomposition Method (FADDM) for our 12×12 TCDA.

presented in [13]–[25], we obtain

$$G_{dB} = G_{0dB} - 10.72 \left(\frac{\lambda_{high} S_{\gamma_m} \sigma_\theta}{\lambda} \right)^2 \quad (22)$$

In the above, G_{0dB} is the maximum achievable gain of the error-free aperture, γ_m is the acute angle of the Miura-ori TCDA, λ_{high} is the wavelength at the highest operating frequency, and σ_θ is the standard deviation of the angular error $\delta\theta$. It is noted that (22) denotes a particular case of the Ruze equation applied to the z-directed errors of a partially deployed Miura-ori TCDA. Also, using (19), the maximum gain in (22) can be rewritten as

$$G_{dB} = G_{0dB} - 171.45 \left(\frac{\epsilon}{\lambda} \right)^2 \quad (23)$$

where $\epsilon = H(\delta\theta_m, \gamma_m)/2$ can be interpreted as the RMS of the z-directed position errors associated with array element folding.

C. VERIFICATION VIA FULL-WAVE SIMULATION

To verify (22), finite simulations of a 12×12 elements TCDA were carried out. Precisely, the proposed array was simulated using the Ansys HFSS built-in Finite Array Domain Decomposition Method (FADDM). With such a method, the mesh of the original unit cell is replicated using classical PBC. Notably, using this method, each element can have a different magnitude and phase. A simulation of the error-free array was first carried out. Then random phase errors were introduced as a post-processing step using a random 12×12 normally distributed phase error matrix generated using (21). The simulation set-up is illustrated in Fig. 10. Fig. 11 compares the gain degradation envelope of 25 array distributions and their empirical average (3600 random errors) with the theoretical gain degradation of (22).

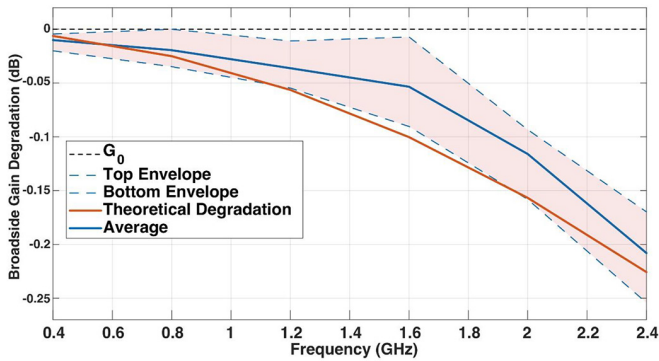


FIGURE 11. Gain degradation envelope for 25 arrays vs the theoretical gain degradation given in (22).

It is observed that the theoretical degradation tends to provide the worst-case scenario degradation. Additionally, several factors can explain the slight discrepancy between the theoretical degradation and full-wave simulations. For example, the derivation leading to (22) assumes that all the elements possess identical embedded element patterns, but this is not the case of the finite array. Additionally, edge effects and mutual coupling between the array elements are not considered. In practice, such consideration cannot be analytically included. On the other hand, the carried-out full-wave simulations account for the ground plane's finite effects and the difference in embedded element patterns.

D. DISCUSSION: COMPENSATION & CALIBRATION METHODS

The approach presented previously only accounts for array elements displacement errors due to physical deformation of Miura-ori apertures. However, spaceborne phased array systems are affected by various errors due to element failure, power amplifiers (amplitude error), phase shifters, thermal distortion, fabrication tolerances. Further, as presented in [13]–[14] deterministic mechanical distortion modes also affect the maximum gain and increase arrays sidelobe levels (SLL). Consequently, the total contribution of such errors unreasonably diminishes the performance of spaceborne apertures. Different compensation methods for mechanical errors have been proposed in the literature.

In [26], Wang *et al.* propose a method to compute compensated excitations amplitude and phase using the Fast Fourier Transform (FFT) algorithm. The proposed method uses a first-order approximation of the array factor subject to small position errors. Using such a model, the Direct Fourier Transform (DFT) of the array factor is computed, and the Fourier weights corresponding to each element are extracted. Further, the array deformation is measured using digital photogrammetry, and the Fourier weights of the deformed array are obtained using the same model, including the measured position errors. Finally, the compensated excitations are obtained with the Inverse Direct Fourier Transform (IDFT) and plugged back in the phased array system.

In [27], de Wit *et al.* propose a concept for measuring and compensating array deformations by attaching several accelerometers and an inertial measurement unit (IMU) to the phased array structure. By combining the measurements of both sensors, the deformations of the array aperture can be characterized, and phase corrections applied.

Alternatively, in [28], Takahashi *et al.* propose an onboard calibration method for mechanical distortions of satellite phased arrays that use probe antenna in the far-field region of the phased array. In this method, the compensation phase is computed using the electrical path between each phased array element and the probe antenna.

V. CONCLUSION

The performance of partially deployed Miura-ori TCDA was investigated in this paper. The presented antenna array analysis led to a closed-form expression for the expected gain degradation caused by angular errors within the origami structure. Notably, the developed gain error includes variations in the key parameters of the Miura-ori array geometry. As the proposed degradation depends on the operating wavelength, the array aperture performance is not affected in the same way throughout the frequency range. For example, at lower frequencies, geometrical errors have less impact as compared to high frequencies. It is remarked that, for the proposed Tightly Coupled Dipole Array (TCDA), the impact is 40 times less at its lowest operating frequency of 0.35 GHz when compared to its gain performance at 2.4 GHz. Finally, the proposed degradation was verified using full-wave simulations. The main limitation of the proposed analysis is the approximation that all the array elements are subject to the same random error. However, in a real-life scenario, the folding of the aperture is likely to be non-uniform, especially for a finite structure where the edges fold more than the center. Accounting for such a scenario would require modeling each face with a different random variable. This could be accomplished by fully characterizing the array mechanical structure as in [29]. However, a simpler method consists of considering the worst-case scenario where an upper bound of the gain degradation could be found by over-evaluating the deformation. That is, considering that all the elements fold as much as the edge elements.

REFERENCES

- [1] E. Kulu, *Nanosats Database 2014–2021*. Accessed: May 20, 2021. [Online]. Available: <https://www.nanosats.eu/>
- [2] E. Hand, "The rise of the CubeSat," *Science*, vol. 346, p. 1449, Dec. 2014. Accessed: May 21, 2021. [Online]. Available: <https://science.sciencemag.org/>
- [3] M. Carvalho, A. D. Johnson, E. A. Alwan, and J. L. Volakis, "Semi-resistive approach for tightly coupled dipole array bandwidth enhancement," *IEEE Open J. Antennas Propag.*, vol. 2, pp. 110–117, 2021.
- [4] E. Peral *et al.*, "Radar technologies for earth remote sensing from CubeSat platforms," *Proc. IEEE*, vol. 106, no. 3, pp. 404–418, Mar. 2018.
- [5] M. Hwang, G. Kim, S. Kim, and N. S. Jeong, "Origami-inspired radiation pattern and shape reconfigurable dipole array antenna at C-band for CubeSat applications," *IEEE Trans. Antennas Propag.*, vol. 69, no. 5, pp. 2697–2705, May 2021.

- [6] N. Miguélez-Gómez *et al.*, “Thickness-accommodation in X-band origami-based reflectarray antenna for small satellites applications,” in *Proc. IEEE Int. Conf. Wireless Space Extreme Environ. (WiSEE)*, Vicenza, Italy, 2020, pp. 54–59.
- [7] M. Arya, “Packaging and deployment of large planar spacecraft structures,” Ph.D. dissertation, Dept. Doctor Philos., California Inst. Technol., Pasadena, CA, USA, 2016.
- [8] Y. Miyazaki, “Deployable techniques for small satellites,” *Proc. IEEE*, vol. 106, no. 3, pp. 471–483, Mar. 2018.
- [9] J. Ruze, “The effect of aperture errors on the antenna radiation pattern,” *Il Nuovo Cimento*, vol. 9, pp. 364–380, Mar. 1952.
- [10] L. L. Bailin and M. J. Ehrlich, “Factors affecting the performance of linear arrays,” *Trans. IRE Prof. Group Antennas Propag.*, vol. 1, no. 1, pp. 85–106, Feb. 1952.
- [11] R. Elliott, “Mechanical and electrical tolerances for two-dimensional scanning antenna arrays,” *IRE Trans. Antennas Propag.*, vol. 6, no. 1, pp. 114–120, Jan. 1958.
- [12] L. Rondinelli, “Effects of random errors on the performance of antenna arrays of many elements,” in *Proc. IRE Int. Conv. Rec.*, vol. 7. New York, NY, USA, 1959, pp. 174–189.
- [13] H. S. C. Wang, “Performance of phased array antennas under error conditions,” in *Proc. IEEE Aerosp. Appl. Conf.*, Breckenridge, CO, USA, 1989, p. 25.
- [14] H. S. C. Wang, “Performance of phased-array antennas with mechanical errors,” *IEEE Trans. Aerosp. Electron. Syst.*, vol. 28, no. 2, pp. 535–545, Apr. 1992.
- [15] P. Zulch, R. Hancock, and J. McKay, “Array deformation performance impacts on a LEO L-band GMTI SBR,” in *Proc. IEEE Aerosp. Conf., Big Sky*, MT, USA, 2005, pp. 2171–2179.
- [16] A. Ossowska, J. H. Kim, and W. Wiesbeck, “Influence of mechanical antenna distortions on the performance of the HRWS SAR system,” in *Proc. IEEE Int. Geosci. Remote Sens. Symp.*, Barcelona, Spain, 2007, pp. 2152–2155.
- [17] B. Y. Dharmadasa, H. M. Y. C. Mallikarachchi, and F. L. Jimenez, “Characterizing the mechanics of fold-lines in thin Kapton membranes,” in *Proc. AIAA Spacecraft Struct. Conf. Amer. Inst. Astronaut. Astronaut.*, Jan. 2018, pp. 1–14.
- [18] S. D. Guest, Deployable structures: Concepts and analysis,” Ph.D. dissertation, Dept. Doctor Philos., Univ. Cambridge, Cambridge, U.K., 1994.
- [19] C. Sickinger and E. Breitbach, “Ultra-lightweight deployable space structures,” in *Proc. 4th Int. Conf. Thin-Walled Struct.*, Jun. 2004, pp. 1–2.
- [20] X. Liu, S. Yao, B. S. Cook, M. M. Tentzeris, and S. V. Georgakopoulos, “An origami reconfigurable axial-mode Bifilar helical antenna,” *IEEE Trans. Antennas Propag.*, vol. 63, no. 12, pp. 5897–5903, Dec. 2015.
- [21] M. Hamza, C. L. Zekios, and S. V. Georgakopoulos, “A thick origami reconfigurable and packable patch array with enhanced beam steering,” *IEEE Trans. Antennas Propag.*, vol. 68, no. 5, pp. 3653–3663, May 2020.
- [22] M. Schenk and S. D. Guest, “Geometry of Miura-folded metamaterials,” *Proc. Nat. Acad. Sci.*, vol. 110, no. 9, pp. 3276–3281, 2013.
- [23] J. P. Doane, K. Sertel, and J. L. Volakis, “Bandwidth limits for lossless, reciprocal PEC-backed arrays of arbitrary polarization,” *IEEE Trans. Antennas Propag.*, vol. 62, no. 5, pp. 2531–2542, May 2014.
- [24] J. Ruze, “Antenna tolerance theory—A review,” *Proc. IEEE*, vol. 54, no. 4, pp. 633–640, Apr. 1966.
- [25] L. D’Addario, “Combining loss of a transmitting array due to phase errors,” *IPN Progr.*, Pasadena, CA, USA, Rep. 42-175, 2008.
- [26] C. Wang, Y. Wang, J. Zhou, M. Wang, J. Zhong, and B. Duan, “Compensation method for distorted planar array antennas based on structural–electromagnetic coupling and fast Fourier transform,” *IET Microw. Antennas Propag.*, vol. 12, pp. 954–962, Feb. 2018.
- [27] J. J. M. de Wit, W. L. van Rossum, M. P. G. Otten, and A. G. P. Koekenberg, “Concept for measuring and compensating array deformation,” in *Proc. Eur. Radar Conf.*, Munich, Germany, 2007, pp. 55–58.
- [28] T. Takahashi *et al.*, “On-board calibration methods for mechanical distortions of satellite phased array antennas,” *IEEE Trans. Antennas Propag.*, vol. 60, no. 3, pp. 1362–1372, Mar. 2012.
- [29] E. Lier, M. Zemlyansky, D. Purdy, and D. Farina, “Phased array calibration and characterization based on orthogonal coding: Theory and experimental validation,” in *Proc. IEEE Int. Symp. Phased Array Syst. Technol.*, Waltham, MA, USA, 2010, pp. 271–278.



MAXENCE CARVALHO (Graduate Student Member, IEEE) was born in Clermont-Ferrand, France, in 1994. He received the M.Sc. degree in aeronautical and spatial telecommunications from the l’École National de l’Aviation Civile, Toulouse, France, in 2018. He is currently pursuing the Ph.D. degree with the RFCOM Lab, Florida International University, Miami, FL, USA. His current research interests include ultra-wideband arrays, millimeter-wave antennas for imaging applications, and reconfigurable antennas. He was the Honorable Mention Award recipient in the Student Paper Competition at the 2021 National Radio Science Meeting.



JOHN L. VOLAKIS (Fellow, IEEE) was born on May 13, 1956 in Chios, Greece and immigrated to the USA in 1973. He received the B.E. degree (*summa cum laude*) from Youngstown State University, Youngstown, OH, USA, in 1978, and the M.Sc. and Ph.D. degree from The Ohio State University, Columbus, OH, USA, in 1979 and 1982, respectively.

He started his career with Rockwell International North American Aircraft Operations from 1982 to 1984, currently Boeing. In 1984, he was appointed as an Assistant Professor with the University of Michigan at Ann Arbor, Ann Arbor, MI, USA, becoming a Full Professor in 1994. He also served as the Director of the Radiation Laboratory from 1998 to 2000. From January 2003 to August 2017, he was the Roy and a Lois Chope Chair Professor of Engineering with Ohio State University, and served as the Director of the ElectroScience Laboratory from 2003 to 2016. Since August 2017, he has been the Dean of the College of Engineering and Computing and a Professor of Electrical and Computer Engineering with Florida International University. He has graduated/mentored 97 doctoral students/post-docs with 43 of them receiving best paper awards at conferences. His publications include eight books, over 440 journal papers and 900 conference papers, 30 book chapters, and 30 patents/disclosures. Among his coauthored books are: *Approximate Boundary Conditions in Electromagnetics* (1995); *Finite Element Methods for Electromagnetics* (1998); *Antenna Engineering Handbook* (Fourth Edition, 2007 and Fifth Edition, 2009); *Small Antennas* (2010); and *Integral Equation Methods for Electromagnetics* (2011). Over the years, he carried out research in computational methods, antennas, wireless communications and propagation, electromagnetic compatibility and interference, design optimization, RF materials, multiphysics engineering, millimeter waves, terahertz and medical sensing.

Prof. Volakis awards are: The University of Michigan College of Engineering Research Excellence Award in 1993, the Scott Award from The Ohio State University College of Engineering for Outstanding Academic Achievement in 2011, the IEEE AP Society C-T. Tai Teaching Excellence Award in 2011, the IEEE Henning Mentoring Award in 2013, the IEEE Antennas & Propagation Distinguished Achievement Award in 2014, The Ohio State University Distinguished Scholar Award in 2016, The Ohio State University ElectroScience Laboratory George Sinclair Award in 2017, and the URSI Booker Gold Medal in 2020. He was listed by ISI among the top 250 most referenced authors in 2004. His service to Professional Societies include: the 2004 President of the IEEE Antennas and Propagation Society in 2004, a Chair of USNC/URSI Commission B from 2015 to 2017, twice the General Chair of the IEEE Antennas and Propagation Symposium, an IEEE APS Distinguished Lecturer, an IEEE APS Fellows Committee Chair, an IEEE-Wide Fellows Committee Member, and an associate editor of several journals. He is the Fellow of the Advanced Computational Electromagnetics Society, American Association for the Advancement of Science, and National Academy of Inventors in 2021.